COMMENT

Efflorescence, subflorescence, and crust weathering characteristics of sandstone in Nankan Grotto, China: insights into petrography and environment constraints

Xuening Zhang[1], Xiyong Wu[1,3], Sixiang Ling[2,3*] and Yijian Cao[2]

Abstract

The different salt weathering issues of the sandstone in the Nankan Grotto have significantly influenced their preservation conditions. This work aimed to evaluate the petrography and environment constraints for salt weathering of three typical sandstones: yellow sandstone, cyan sandstone, and gray sandstone in the Nankan Grotto. Salt resistance test and acid leaching test were conducted on these three sandstones. In addition, the mineralogy, geochemical mass balance, micro-structure, and water transport properties of these sandstones were also analyzed. It is found that yellow sandstone had high quartz concentration, porosity, and water transport ability. Cyan sandstone had low calcite concentration, high porosity and medium water transport ability. Gray sandstone had high calcite concentration, low porosity and water transport ability. The decay of sandstones in the salt resistance test at 20 °C was faster than those at 5 °C and 35 °C. In addition, yellow sandstone was the most resistant to the salt resistance test, followed by cyan sandstone, and gray sandstone was the most vulnerable to the salt resistance test. In the H_2SO_4 acid leaching test, efflorescence pattern was the most likely type of decay in yellow and cyan sandstones. Thenardite was the exclusive salt in the yellow sandstone, while gypsum was the mainly salt in the cyan sandstone. Gypsum crust and subflorescence were the most common types of decay for gray sandstone. In the HNO_3 acid leaching test, yellow and cyan sandstones did not show obvious variations. For gray sandstone, the secondary minerals were gypsum and dolomite, and crust pattern was observed. In general, the salt weathering of gray sandstone was more severe than yellow and cyan sandstones. The differences in petrography (mainly calcite concentration) and micro-structure of sandstone and the external environment leaded to the differences in the types, amounts, and locations of the salt crystallization in the acid leaching tests. These contributed to the different development of efflorescence, subflorescence, and crust patterns. Our research reveals the petrographic, micro-structural, and environmental constraints for different salt weathering processes of sandstones in the Nankan Grotto.

Keywords Sandstone heritage, Salt weathering, Petrography, Micro-structure, Environment

*Correspondence:
Sixiang Ling
lingsx@swjtu.edu.cn
Full list of author information is available at the end of the article

Zhang *et al. Heritage Science*   (2024) 12:244

Page 2 of 16

Introduction

Sandstone monuments are important parts of our world's cultural heritage and represent the diverse artistic, historical, and scientific achievements of humans [1]. They have undergone various degrees of decay over long geological timescales under the combined influences of internal factors, such as petrography and sedimentology characteristics [2–4], and external factors, such as environmental, geological and anthropogenic disturbances [5–8]. Notably, salt weathering is one of the main processes causing severe decay in sandstone, which has been repeatedly investigated at some international heritage sites [9–11].

It is widely accepted that salt weathering mechanisms of sandstone are controlled by its petrography and the external environment [12]. The petrographic characteristic of the sandstone determined the concentration and mixture of ions in the solution, which further determined the type of salt and its amount [13, 14]. In addition, the micro-structure of sandstone, such as pore volume, size distribution, shape, and degree of interconnection, controlled the mode and rate of solution transport and retention [15–18]. At the same time, the environmental conditions (such as temperature and relative humidity) controlled the drying kinetics of the solution [19–21]. These factors determined whether the salts would crystallize at the surface as efflorescence/crust or inside the material as damaging subflorescence [14].

The weathering mechanisms of salt weathering in the Nankan Grotto have been preliminarily explored: Thenardite and calcite crystallized inside the rock, resulting in the formation of the subflorescence pattern. The precipitation of gypsum and calcite on the surface resulted in the formation of the crust pattern [22]. We found that the difference in the mineralogy (especially the calcite content) of the sandstone laid the foundation for the distinct development of subflorescence and crust patterns. However, the micro-structural and environmental influences leading to the differentiation of salt weathering in the Nankan Grotto are still unclear.

Here, we designed salt resistance test and acid leaching test for the three sandstones from the Nankan Grotto. The sandstone samples before and after-test were collected to analyze the mineralogy, major element, petrophysical properties, and micro-structure. The main objectives of this study were (i) to verify the influence of petrography to the distinct development of efflorescence, subflorescence, and crust patterns in the Nankan Grotto, (ii) to investigate the micro-structural influences for salt weathering of the sandstone in the Nankan Grotto, and (iii) to elucidate the environmental influences that leading to rock deterioration differentiation. The results of this study provide new insights that improve our knowledges of the salt weathering processes in sandstone grotto heritage sites.

Study site and sampling

The Nankan Grotto is located in Bazhong City, Sichuan Province (Fig. 1a). The existing sandstone grottoes are clustered in the Giant Buddha Cave Area (Fig. 1b). The average annual temperature of Bazhong City is approximately 16 °C, with the lowest average daily temperature of 6.1 °C in January and the highest one of 27.1 °C in July. There are approximately 12–15 days per year of high temperature, reaching temperature extremes above 35 °C. The annual relative humidity varies from 64 to 84% [23, 24].

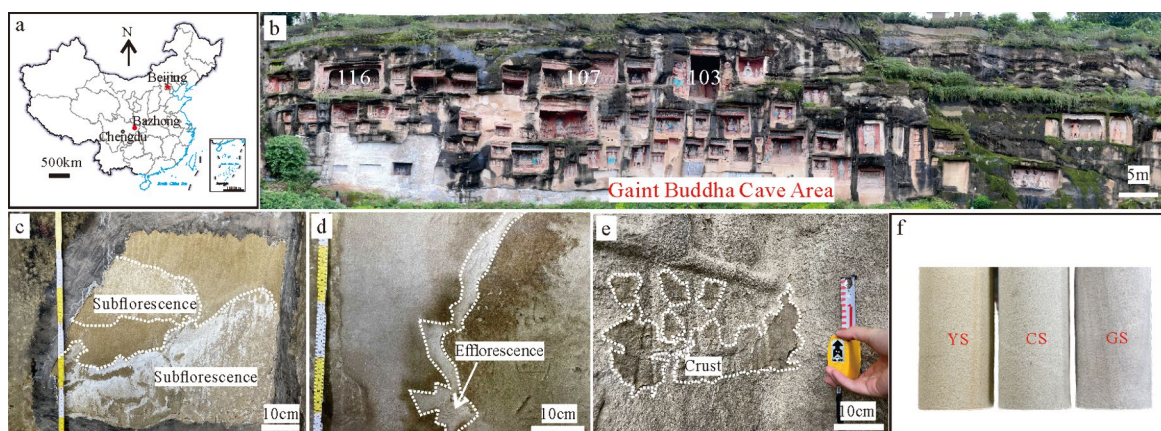**Fig. 1** Field observations and different deterioration patterns in the Nankan Grotto. **a** Location of the study area. **b** Field photograph of the Giant Buddha Cave Area. The Arabic numerals are the sequential numbers of the Buddhas. **c** Subflorescence pattern. **d** Efflorescence pattern. **e** Crust pattern. **f** Three types of sandstone samples for geochemical and petrophysical analyses

Zhang *et al. Heritage Science*   (2024) 12:244

Page 3 of 16

Subflorescence corresponds to salt crystallization in the material pores and under the stone surface. Subflorescences are also visible on the newly exposed surface when the stone layer over them was detached (Fig. 1c). Efflorescences are generally poorly bonded to the stone surface and not suspected to cause severe damage to the material than subflorescence (Fig. 1d). Crust was hard, and its color was brown or dark brown, including the products of extraneous sedimentary materials and secondary mineralization (Fig. 1e). In the Nankan Grotto, the compositions of subflorescence and efflorescence were mainly thenardite (Na_2SO_4), and the composition of crust was mainly gypsum ($CaSO_4 \cdot 2H_2O$) [22].

The experimental samples for geochemical and petrophysical analyses were fresh sandstones, which belong to the Lower Cretaceous Bailong Formation. Based on the apparent particle size and color, the collected sandstone can be divided into three types: yellow sandstone (named YS), cyan sandstone (named CS), and gray sandstone (named GS) (Fig. 1f). YS, CS, and GS were collected from the bottom, middle, and top of the stratum in the Giant Buddha Cave Area. In the Nankan Grotto, subflorescence pattern developed in YS (Fig. 1c), efflorescence pattern developed in CS sandstone (Fig. 1d), and crust pattern developed in GS sandstone (Fig. 1e).

Methods
Salt resistance test
Three types sandstone samples were subjected to a salt resistance test adapted from Angeli [25]. Thenardite was detected in the subflorescence in the Nankan Grotto [22]. In addition, sodium sulfate was well known as an extremely damaging salt from numerous laboratory tests and case studies in the stone deterioration processes [26, 27]. Therefore, sodium sulfate was used in the salt resistance test. The test was run under three different ambient temperatures: 5 °C, 20 °C, and 35 °C, with a constant relative humidity of 75% (Fig. 2a). Each cubic sample (30×30×30 mm) underwent a salt crystallization test with cycles. Each cycle had a duration of 24 h, following three steps:

  i.   4 h total immersion in a 0.5 mol/L Na_2SO_4 aqueous solution at an ambient temperature, i.e. 5 °C, 20 °C, or 35 °C,
  ii. 16 h oven drying at 105 °C,
  iii. 4 h cooling at initial ambient temperature.

The samples were weighed three times during the cycles: before imbibition, after imbibition, and after drying. The salt remaining in the samples was not removed before weighting, that is, the measured weight was the total of the rock sample and the salt remained in the pores. The sample size was 40×40×40 mm in Angeli [25], and the immersion and cooling times were 2 h and 7 h, respectively. The sample size was 30×30×30 mm in this study, and the immersion and cooling times were 4 h and 4 h, respectively. The extended immersion time and smaller sample size were aimed at allowing the sodium sulfate solution to penetrate deeper into the samples.

Acid leaching test
Additionally, acid leaching tests were designed. Each cubic sample (30×30×30 mm) was placed on a permeable-stone slice (Φ65×10 mm). They were placed in a solution container with 0.01 mol/L H_2SO_4 or 0.01 mol/L HNO_3 solutions (Fig. 2b). The H_2SO_4 solution was used to simulate the deterioration process of fresh sandstone by providing SO_4^{2-} to form sulfate. The HNO_3 solution was used to provide acid condition and did not provide exogenetic SO_4^{2-}. After the tests, the secondary minerals on the samples surface were collected by tweezers for mineralogical analysis. The salt resistance test and acid leaching test were conducted on parallel samples to eliminate accidental errors.

Petrographic characteristics and mineralogical analysis
Each sample with a diameter of Φ25 mm×5 mm was vacuum impregnated with blue epoxy to highlight the void spaces. Then, thin sections were cut. The sections were ground to a thickness of 30 μm and polished using polishing fluid (Cr_2O_3 and $(NH_4)_2Cr_2O_7$) and a polishing machine. The petrographic characteristics were visualized under plane-polarized light and reflected light using an Olympus CX43 optical microscope.

The mineralogical compositions of the samples were determined via X-ray diffraction (XRD) using Cu-Kα radiation (Bruker D8 DISCOVER, Germany; 40 kV; 40 mA; λ=1.54059 Å). The detailed analysis procedures refer to previously published methods [28]. The whole rock samples were analysed from 2θ angles of 5° to 45° and a step size of 0.02°/sec. The clay fractions were extracted from whole rock sample as described by Ling et al. [28]. Then, the clay fractions were further treated via (i) air drying; (ii) the addition of ethylene glycol; and (iii) thermal-processing at 450 °C. All of the treated clay samples were analysed by XRD from 2.5° to 30° (2θ) with a step size of 0.02°/sec. The mineral contents were quantified using whole pattern fitting and Rietveld refinement. The relative standard deviation (RSD) of the XRD measurements was less than 10%. The lowest detection limit was 0.1 wt%.

Major element analysis
The major element compositions were analysed via X-ray fluorescence spectroscopy (XRF; PANalytical PW2424,

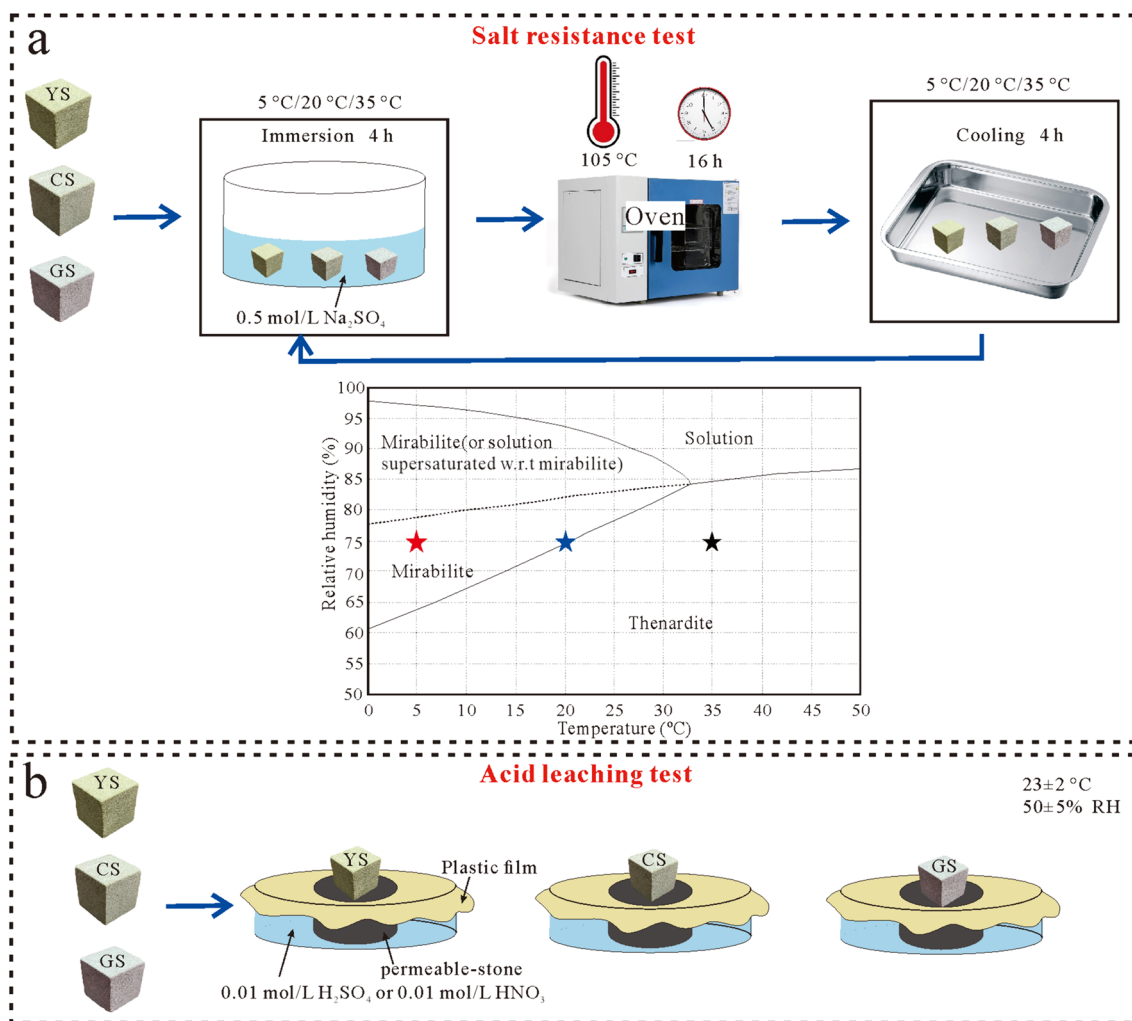Zhang *et al. Heritage Science*   (2024) 12:244

Page 4 of 16

Fig. 2 Tests flow chat. **a** salt resistance test. Red, blue, and black stars represent the three temperature and humidity conditions in the salt resistance test. **b** acid leaching test

Netherlands). For the chemical analysis, two powdered samples were weighed for each sample. One sample was fused with $LiBO_2$-$Li_2B_4O_7$ flux and an oxidizing agent ($LiNO_3$), which detail described in Ling et al. [29]. Then, the melted sample was poured into a platinum mold and prepared for XRF analysis. Another sample was calcined in a muffle furnace with oxygen at 1000 ℃ to calculate the loss on ignition (LOI). Measurements were carried out on standard and parallel samples, and the relative deviation (RD) and relative error (RE) of the XRF measurements were less than 5%. The lowest detection limit was 0.01%.

Density, porosity and water transport properties measurements

Density was measured as the ratio between dry mass and bulk volume of the sample ($\Phi50\times100$ mm) in accordance with the GB/T 50266 standard [30]. Before the measurements, the samples were completely dried in a drying oven at 105 ℃ to a constant mass. For the oven-dried samples, the dry mass was weighed and the apparent volume was measured on the basis of its dimension.

The porosity and pore size distribution were determined by mercury intrusion porosimetry (MIP, Micromeretics AutoPore IV 9505, America). Before the measurements, the samples were cut into centimeter size and heated at 105 ℃ for 24 h under high vacuum conditions. Then, mercury was intruded into the pore volume at discrete pressure steps until the maximum pressure of 200 MPa was reached. The adopted pore size classification was: micropores (<10 nm), transition-pores (10–100 nm), mesopores (0.1–1 μm), and macropores (>1 μm).

Zhang *et al. Heritage Science*   (2024) 12:244

Page 5 of 16

Unforced water absorption was carried out on the samples ($\Phi 50 \times 50$ mm) in accordance with the GB/T 50266 standard [30]. All of the samples were completely dried in a drying oven at 105 °C to eliminate the existing moisture. Then, the samples were immersed completely in distilled water for 48 h at atmospheric pressure. Water absorption under atmospheric pressure was expressed as the mass ratio of absorbed water and oven-dried sample in form of percentage.

Capillary water uptake was determined by continuous measurements of the sample weight and the height of water uptake in accordance with the GB/T 9966.13 standard [31]. The cylindrical samples ($\Phi 50 \times 100$ mm) were placed vertically on a permeable-stone slice ($\Phi 65 \times 10$ mm), then they were placed on an electronic balance with a 0.01 g resolution connected to a computer for the data acquisition. A container with deionized water was then raised, until the water touched the top surface of the permeable-stone. The water uptake in the sandstone sample was constrained along the vertical direction. The bedding plane of sample was horizontal, that is, the direction of capillary water uptake was vertical to the bedding plane. The settings were placed in a climate chamber with constant temperature (23 ± 2 °C) and relative humidity ($50 \pm 5\%$).

Apart from capillary absorption, water vapour diffusion is the second most important water transport mechanism in porous material [32]. The water vapour diffusion value of the sandstone sample was measured using the wet-cup method in accordance with the GB/T 17146 standard [33]. Slice of each sample ($\Phi 50 \times 10$ mm) was sealed as cover on teflon cup and connected with a distilled water reservoir by a large cotton wick. Then, the cups were placed in a climate chamber with constant temperature (23 ± 2 °C) and relative humidity ($50 \pm 5\%$). This caused moisture to flow through the porous material from the inside (100% RH) to the outside (50% RH). The water vapour diffusion values were obtained by weighing the cups periodically. The bedding plane of sample was horizontal, that is, the direction of water vapour diffusion was vertical to the bedding plane. In the capillary water uptake and water vapour diffusion tests, the anisotropy of sandstone was not taken into account.

Evaporative drying was determined by continuous weighting of the samples. Firstly, the cylindrical samples ($\Phi 50 \times 100$ mm) were impregnated with distilled water for 48 h until reaching constant weight. Then, the cylindrical samples were drying through their top and side surface under controlled environmental conditions (23 ± 2 °C, $50 \pm 5\%$ RH). Meanwhile, the loss of water was monitored by periodical weighing the sample.

Scanning electron microscopy

The microscopic images of the samples were observed via a tungsten filament scanning electron microscope (SEM, JSM-IT500, Japan) with an accelerating voltage of 10 kV. The samples were coated with platinum (Emitech SC7620 sputter coater) prior to observation. The elemental compositions of the selected mineral grains were analysed via an Oxford ULTIM Max 40 EDS system.

Physical and geochemical characteristics of sandstones

Petrographic characteristics and mineralogy of the sandstone

YS, CS and GS have good sorting and medium roundness (Fig. 3a–c). The main mineral of them was quartz, followed by feldspar, calcite, and matrix. YS was fine feldspathic sandstone with grain size around 150–250 μm. CS was fine feldspathic sandstone with grain size around 100–150 μm. GS was very fine feldspathic sandstone with grain size around 50–100 μm.

The XRD analysis results of YS, CS and GS are shown in Table 1. For YS, CS and GS, the quartz concentrations were the highest (63.7–70.7 wt.%), followed by the feldspar (17.6–29.7 wt.%), calcite (1.8–10.0 wt.%), and clay mineral (3.2–8.8 wt.%). The clay minerals were mainly

Fig. 3 Optical microscope images of YS, CS, and GS. **a** Optical microscope image of YS. **b** Optical microscope image of CS. **c** Optical microscope image of GS

Zhang *et al. Heritage Science*   (2024) 12:244

Page 6 of 16

Table 1 Mineral compositions (wt.%) of the samples determined by XRD

Sample name	Quartz	Feldspar	Calcite	Illite–Smectite mixed layer	Illite	Chlorite
YS	70.7	24.8	–	1.9	2.3	0.3
CS	65.3	29.7	1.8	2.4	0.3	0.5
GS	63.7	17.6	10.0	7.7	0.7	0.4
S4*	64.2	22.3	5.1	3.8	2.9	0.7
D4*	62.5	20.2	9.2	3.8	2.3	0.3
S2#	78.9	14.6	2.0	2.1	1.4	0.5
C2#	74.1	14.4	6.1	3.4	1.3	0.3

"–" means the concentration below detection limit 0.1 wt%

S4* and D4* were fresh sandstone samples in the scaling and disintegration pattern sites in the Nankan Grotto, respectively [24]

S2# and C2# were fresh sandstone samples in the subflorescence and crust pattern sites in the Nankan Grotto, respectively [22]

Table 2 Major element compositions (%) of the different sandstones determined by XRF

Sandstone	SiO_2	Al_2O_3	CaO	TFe_2O_3	K_2O	Na_2O	MgO	MnO	P_2O_5	SO_3	TiO_2	LOI
YS	83.16	8.29	0.49	2.09	1.79	1.70	0.78	0.03	0.06	–	0.37	1.91
CS	80.61	8.19	1.44	1.84	1.89	1.76	0.92	0.02	0.04	0.01	0.26	2.46
GS	74.63	8.54	5.25	1.90	1.82	1.68	0.90	0.05	0.07	0.02	0.35	5.43
S4*	73.10	8.86	4.18	3.57	1.79	1.76	1.10	0.05	0.08	0.01	0.39	4.61
D4*	68.84	8.44	8.04	1.94	1.95	1.67	0.73	0.07	0.05	0..01	0.23	7.81
S2#	80.53	7.95	2.27	1.72	1.69	1.62	0.92	0.04	0.05	0.03	0.43	2.82
C2#	76.47	7.52	5.34	1.06	1.71	1.48	0.75	0.04	0.05	0.01	0.20	5.24

"-" means the concentration below detection limit 0.01%

illite–smectite mixed layer (1.9–7.7 wt.%) and illite (0.3–2.3 wt.%), with minor chlorite (0.3–0.5 wt.%).

The quartz and feldspar concentrations of YS, CS, and GS were similar with S4* and D4* samples in the Nankan Grotto. Especially, the quartz, calcite, and feldspar concentrations of GS were very similar with D4*. Compared with S2# and C2#, YS, CS and GS had lower quartz concentration and higher feldspar concentration. GS had the highest calcite and illite–smectite mixed layer concentrations in all of the samples. Calcite was not detected in YS.

Major element compositions

The major element compositions are summarized in Table 2. For YS, CS and GS, SiO_2 concentration (74.63–83.16%) were the highest, followed by the Al_2O_3 (8.19–8.54%), CaO (0.49–5.25%), Fe_2O_3 (1.84–2.09%), K_2O (1.79–1.89%), and Na_2O (1.68–1.76%) concentrations. The concentrations of the other oxides, such as MgO (0.78–0.92%), MnO (0.02–0.05%), P_2O_5 (0.04–0.07%), SO_3 (0.01–0.02%), and TiO_2 (0.26–0.37%), were less than 1.0%. YS showed the highest SiO_2 concentration (83.16%) and the lowest CaO concentration (0.49%).

The major element compositions of YS, CS and GS were different with S4* and D4*. The major element

Table 3 Porosity and water transport properties of different sandstone samples

Sandstone	Density (g/cm³)	Porosity (%)	Unforced water absorption (wt.%)
YS	2.04	9.68	5.49
CS	2.15	9.21	5.26
GS	2.35	7.62	4.52
S4*	/	11.03	/
D4*	/	11.90	/
S2#	/	13.58	/
C2#	/	9.29	/
YG[a]	2.44	9.64	3.16
DZ[a]	2.38	7.69	2.31
LS[a]	2.33	13.02	3.34

YG[a], DZ[a], and LS[a] were fresh sandstone samples in the Yungang Grottoes, Dazu Rock Carvings and Leshan Grand Buddha, respectively [34]

compositions of CS were similar with S2#. The major element compositions of GS were similar with C2#.

Density, porosity and water transport properties

The results of density, porosity and water transport properties of YS, CS, and GS are shown in Table 3 and Figs. 4,
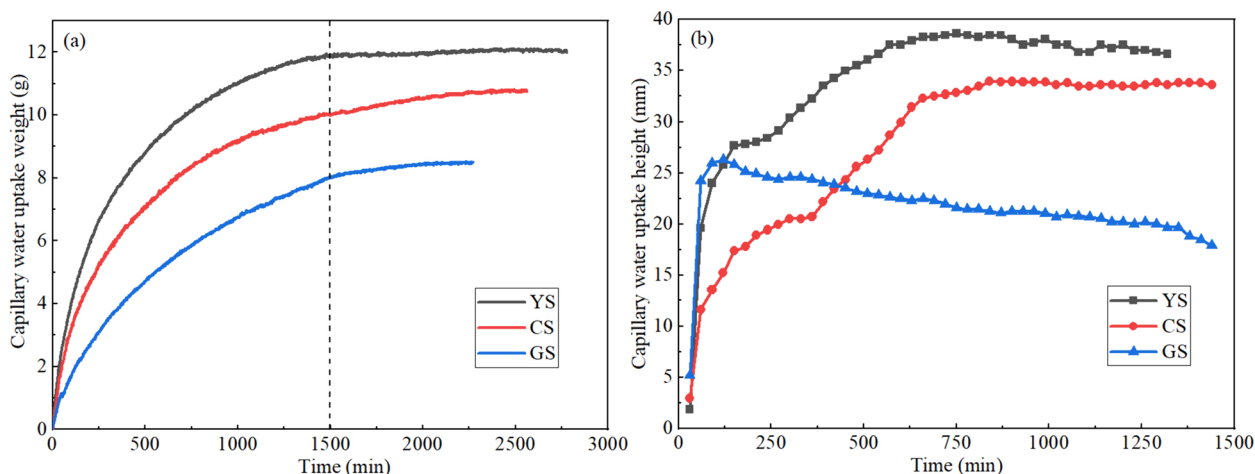
Zhang *et al. Heritage Science*   (2024) 12:244

Page 7 of 16

Fig. 4 Capillary water uptake values of YS, CS, and GS. **a** capillary water uptake weight vs. time. **b** capillary water uptake height vs. time

5. YS and CS had similar properties of density, porosity, and unforced water absorption. However, GS had a higher density, and lower porosity and unforced water absorption than YS and CS.

The densities of YS, CS, and GS were slightly lower than YG^, DZ^, and LS^. The porosities of YS and CS were similar with those of C2# and YG^. The porosity of GS was similar with that of DZ^. The unforced water absorption values of YS, CS, and GS were higher than those of YG^, DZ^, and LS^.

The capillary water uptake weights of YS, CS, and GS were 13.2 g, 11.18 g, and 7.79 g, respectively. The capillary water uptake ratios (the ratio between the capillary water uptake weight and the dry mass of the sample) of YS, CS, and GS were 3.15 wt.%, 2.53 wt.%, and 1.68 wt.%, far away from their unforced water absorption ratios. The curves of capillary water uptake weight for YS, CS, and

GS were homogeneous (Fig. 4a). At the beginning of the test, the amount of capillary water uptake increased fast for all of the three sandstones. Afterwards, the speed of increase gradually slowed down over time until a constant state at approximately 1500 min. The max capillary water uptake heights of YS, CS, and GS were approximately 38 mm, 33 mm, and 26 mm. The curve of capillary water uptake height of YS showed four stages: (i) sharp increase in 0–125 min; (ii) very slow increase in 125–250 min; (iii) steady increase in 250–750 min; (iv) slow decrease in 750–1320 min. The curve of capillary water uptake height of CS also showed four stages: (i) sharp increase in 0–250 min; (ii) very slow increase in 250–375 min; (iii) steady increase in 375–625 min; (iv) being constant in 625–1590 min. The curve of capillary water uptake height of GS showed two stages: (i) sharp increase in 0–125 min; (ii) slow decrease in 125–1470 min
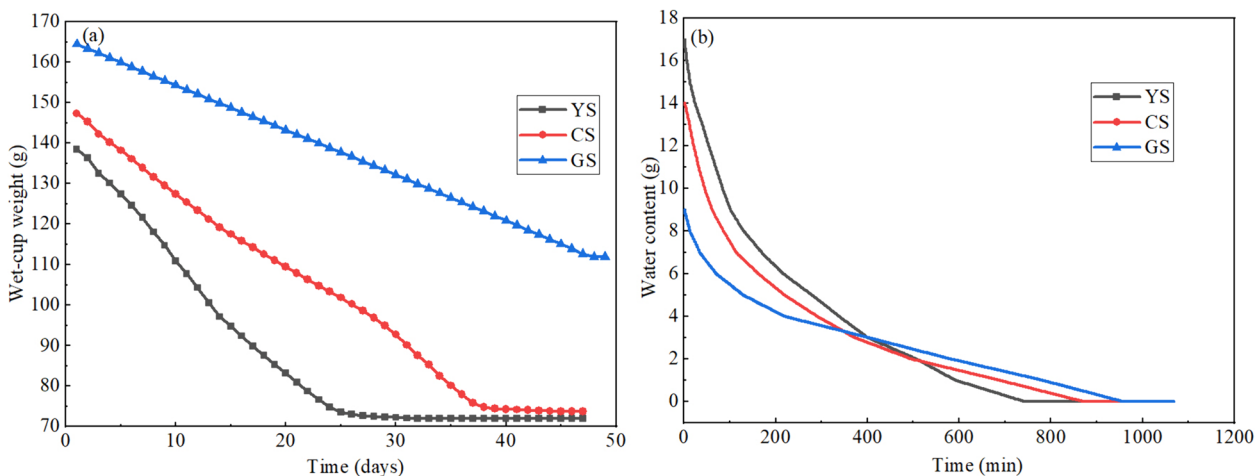

Fig. 5 Water vapour diffusion test and evaporative drying test for YS, CS, and GS. **a** water vapour diffusion curve. **b** evaporative drying curve

Zhang *et al. Heritage Science*   (2024) 12:244

Page 8 of 16

(Fig. 4b). At the beginning of the experiment, the rate of water uptake was fast compared with the rate of evaporation in the lower part of the sample, so that there was a fast water level rise on the surface of the GS. Then, the sample continued to absorb water slowly. GS was very fine sandstone with low porosity, leading to its poor water transport ability. When the water on the surface evaporated, the water in the interior cannot replenish outside timely. Thus, the water in the interior was hardly affected by surface evaporation and still accumulated, leading to the increase of weight. When the water level reached a certain height, the evaporation rate at that height was faster than water uptake rate as time going on, so that the water level on the surface decreased slowly.

The curves of water vapour diffusion for YS, CS, and GS were shown in Fig. 5a. Their slopes reflected the vapour transport ability of porous sandstones. The water vapour diffusion ability showed the best in YS, followed by CS, and showed the worst in GS. The results of capillary water uptake and water vapour diffusion tests only represented the capillary water uptake and water vapour diffusion abilities that perpendicular to the bedding plane. The anisotropy of sandstone was not taken into account.

The losses of water content during evaporative drying for YS, CS, and GS were shown in Fig. 5b. YS showed the highest evaporative drying rate, followed by CS. GS showed the lowest evaporative drying rate.

Results of salt resistance test

The sodium sulfate salt resistance tests for the three sandstones were shown in Figs. 6–8. The decay of all of the samples started after third cycle. The decay processes of sandstones under the three temperatures were different.

At 5 °C, the deterioration patterns of YS, CS, and GS were rounding and crumbling (Fig. 6). At the 5th cycle for YS, CS, and GS, rounding started to appear on the corners and edges of the samples. As the number of cycles increased, the corners and edges smoothed off and the cubes turned into sphere. The rounding and crumbling continued throughout the cycles, and the lost particles formed fine powders.

At 20 °C, the deterioration patterns of YS, CS, and GS were contour scaling and crumbling (Fig. 7). At the 5th cycle for CS and the 6th cycle for YS and GS, contour scaling started to appear, with the detached part thickness of 2–3 mm. The contour scaling turned into crumbling at 7th and 8th cycle for YS and GS.

At 35 °C, the deterioration patterns of YS, CS, and GS were crack and fragmentation (Fig. 8). At the 5th cycle for CS and the 6th cycle for YS, crack started to appear on the sandstone surface. The crack turned into fragmentation from 8th cycle for CS and 9th cycle for YS. GS showed obvious decay from the 5th cycle.

These differences in decay process also reflected a variability in the weight loss schedule. Notably, the trapped salts were not washed away from the samples, which
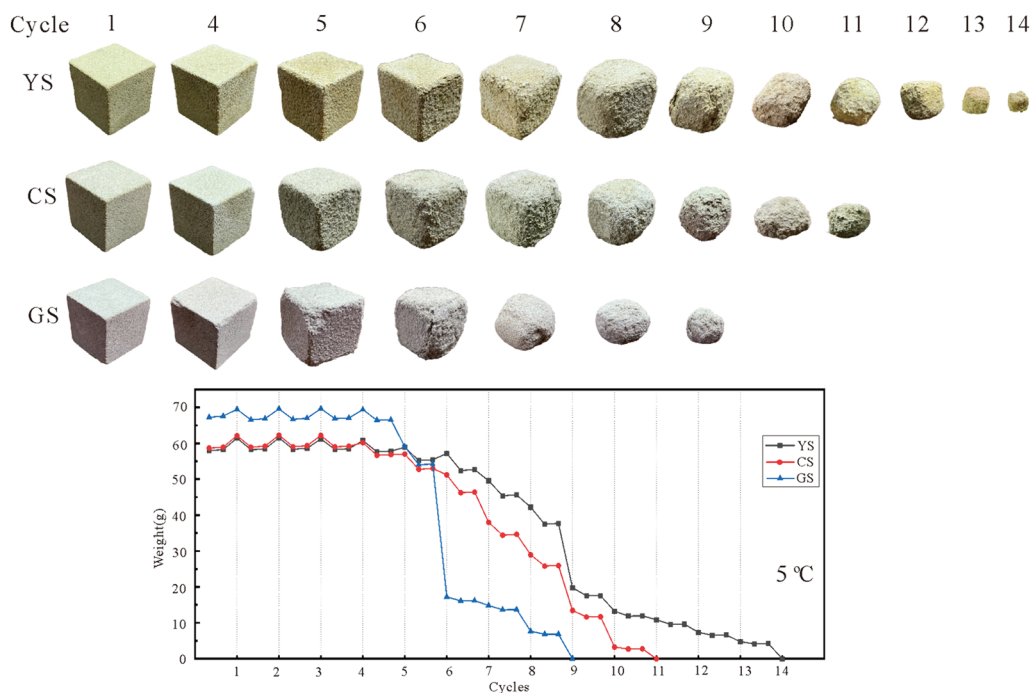

Fig. 6 Salt resistance test for YS, CS, and GS under 5 °C

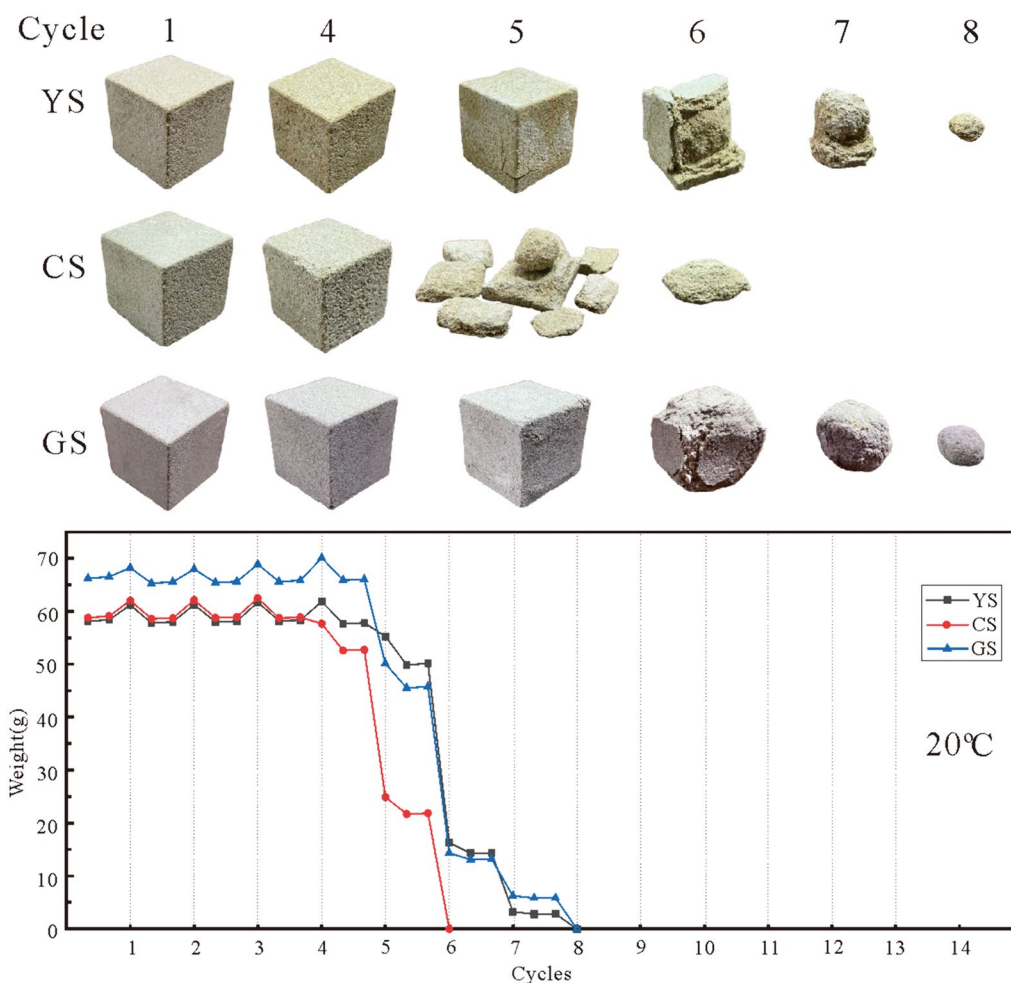Zhang *et al. Heritage Science*   (2024) 12:244

Page 9 of 16

Fig. 7 Salt resistance test for YS, CS, and GS under 20 °C

resulted in that the weight showed a slight increasing trend in the first few cycles in Figs. 6–8. The weight loss of sandstones at 20 °C was faster than those at 5 °C and 35 °C. At 5 °C and 35 °C, the weight loss of GS was the fastest, followed by CS and YS. At 20 °C, the weight loss of CS was the fastest, and the weight loss of YS and GS were similar. In general, YS was the most resistant to the salt resistance test at 5 °C, 20 °C, and 35 °C. GS was the most vulnerable to the salt resistance test at 5 °C and 35 °C.

Results of acid leaching test
Acid leaching test (phenomenon after acid leaching test)

Acid leaching test using 0.01 mol/L H_2SO_4 solution (H_2SO_4 acid leaching test) for YS, CS, and GS was shown in Fig. 9. For YS, fine thenardite (Na_2SO_4) crystals firstly occurred on the edges and corners of the cube at 15th day. Then, thenardite efflorescences were observed on the side of the cube at 45th day, and on the top of the cube at

75th and 105th day. For CS, gypsum crystals occurred on the corners of the cube at 15th day. Then, gypsum efflorescences were located on the side of the cube at 45th day and 75th day, and on the top of the cube at 105th day. For GS, white gypsum crystallized in the corner of the cube at 15th day. This phenomenon was called subflorescence, which resulted in the slight swelling of the corner. At 45th day and 75th day, the swelling of corners increased and gypsum efflorescences were observed on the side of the cube. At 105th day, the top surface swelled obviously and gypsum crust formed on the top surface. For YS, the capillary water uptake height (38 mm) was higher than the cube height in the H_2SO_4 acid leaching test. Therefore, thenardite mainly crystallized on the top surface of the cube. The capillary water uptake height (26 mm) for GS was lower than the cube height, so that gypsum crystallized in the lower half of the cube or combined with primary minerals below the top surface. The capillary water uptake height of CS was between YS and GS, hence
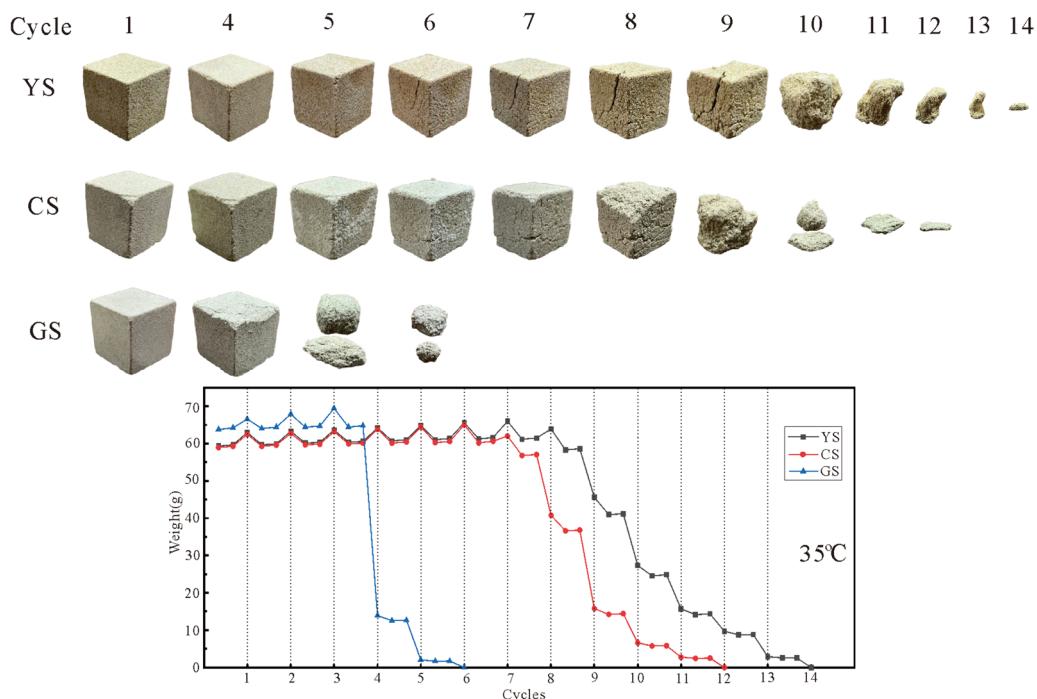
Zhang *et al. Heritage Science*   (2024) 12:244

Page 10 of 16

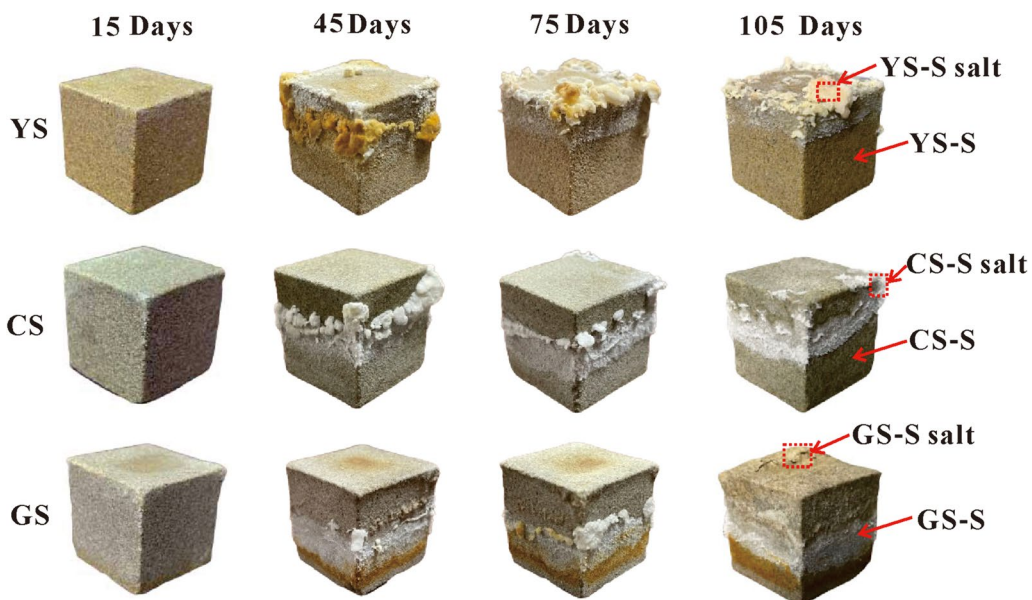**Fig. 8** Salt resistance test for YS, CS, and GS under 35 °C

Fig. 9 H_2SO_4 acid leaching test for YS, CS, and GS

the gypsum accumulation level in CS was in the middle and upper part of the cube.

Acid leaching test using 0.01 mol/L HNO_3 solution (HNO_3 acid leaching test) for YS, CS, and GS was shown in Fig. 10. For YS and CS, there were not obvious

variations until 105th day, except few white crystals occurred on the edges and surfaces of the cubes. For GS, the color of top surface firstly changed at 2nd day. Gypsum crust was observed on the top surface of the cube at 15th day. At 45th, 75th, and 105th day, the gypsum crust had not increased than that at 15th day.
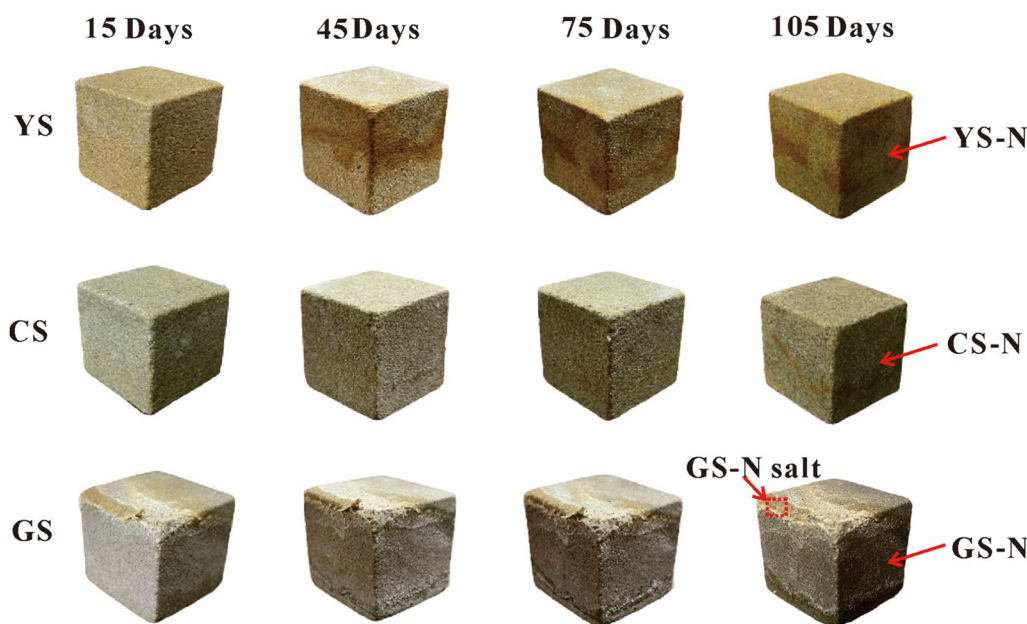
Zhang *et al. Heritage Science*   (2024) 12:244

Page 11 of 16

Fig. 10 HNO$_3$ acid leaching test for YS, CS, and GS

Mineralogy of the secondary minerals in the acid leaching tests

The XRD analysis results of secondary minerals (named samples YS-S salt, CS-S salt, and GS-S salt in Fig. 9 and GS-N salt in Fig. 10) are shown in Table 4. In the H$_2$SO$_4$ acid leaching test, the secondary mineral in sample YS-S was thenardite. The secondary mineral in samples CS-S and GS-S was gypsum. In the HNO$_3$ acid leaching test, the secondary minerals in sample GS-N were gypsum and dolomite.

Pore size distribution under acid leaching test

The pore size distribution frequency of YS, CS and GS and samples after H$_2$SO$_4$/HNO$_3$ acid leaching test (named samples YS-S, CS-S, and GS-S in Fig. 9 and YS-N, CS-N, and GS-N in Fig. 10) are shown in Fig. 11. The measured porosities of YS and CS were 9.68% and 9.21%, respectively. The proportion of macropores approximately accounted for half of the pores in YS and CS, followed by the mesopores, transition-pores, and

micropores. The measured porosity of GS was 7.62%. Mesopores were the dominant pores in GS.

The measured porosity of sample YS-N was 11.80%, and the proportion of macropores accounted for half of the pores. Compared with YS, the numbers of micropores, transition-pores, mesopores, and macropores in sample YS-N all increased. The measured porosity of sample CS-N was 13.78%. Macropores were the dominant pores in sample CS-N, and the number of macropores increased distinctly compared with those in CS. The measured porosity of sample GS-N was 8.53%. Macropores accounted for half of the pores in sample GS-N, and the number of macropores increased obviously compared with those of GS.

The measured porosity of sample YS-S was 15.44%, and the proportion of macropores accounted for half of the pores. Compared with YS, the sharp increase of porosity in sample YS-S was due to the increases of mesopores and macropores. The measured porosity of sample CS-S was 11.05%. The proportions of

Table 4 Mineral compositions (wt.%) of the samples determined by XRD

Sample name	Quartz	Feldspar	Calcite	Gypsum	Dolomite	Smectite	Thenardite	Else
YS-S salt	–	–	–	–	–	–	95.0	5.0
CS-S salt	5.7	–	–	91.8	–	–	–	2.5
GS-S salt	57.2	14.7	2.0	9.5	–	14.6	–	2.0
GS-N salt	15.3	22.4	3.4	50.1	7.8	–	–	1.1

"–" means the concentration below detection limit 0.1 wt.%

"Else" means the concentration of amorphous minerals

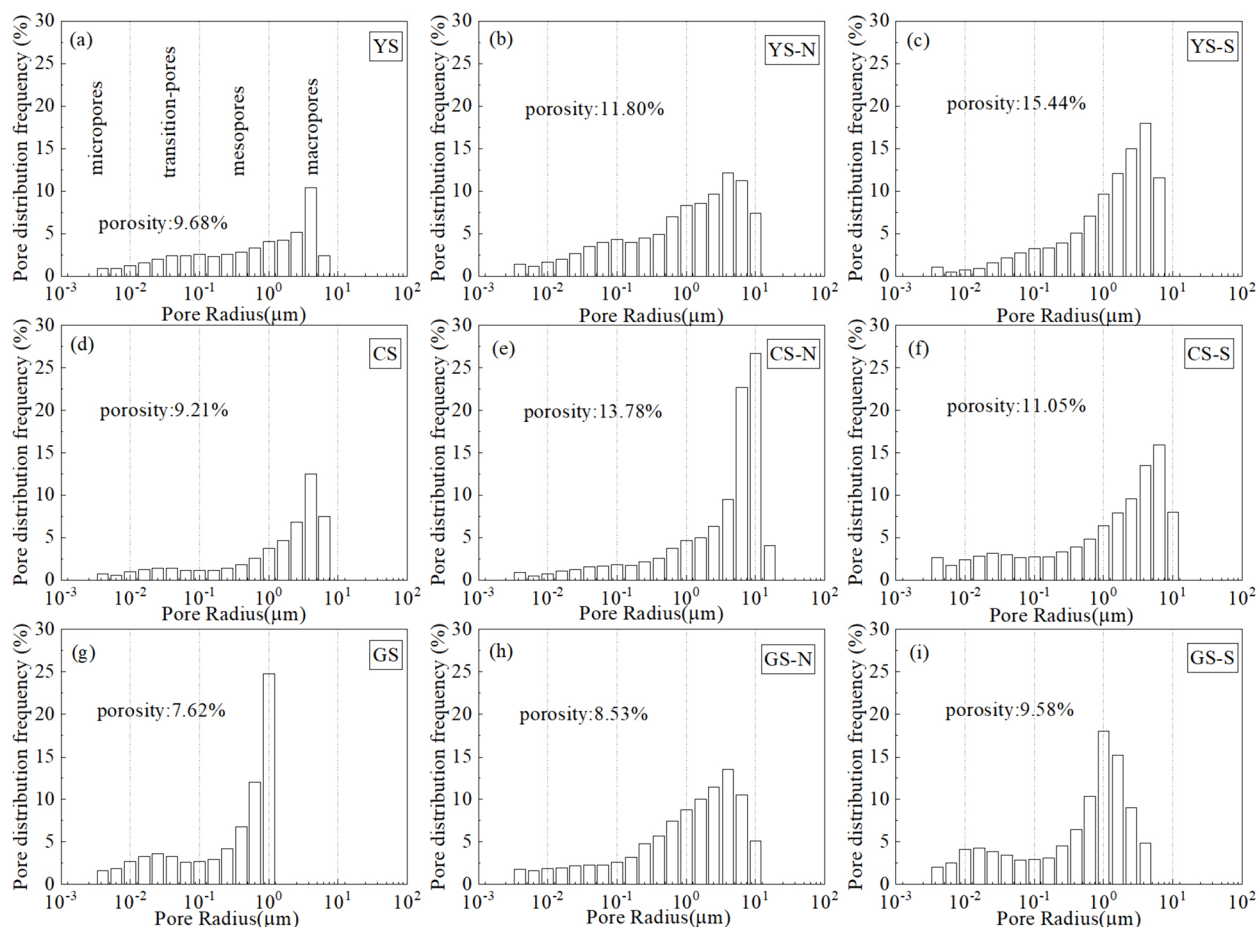Zhang *et al. Heritage Science*   (2024) 12:244

Page 12 of 16

Fig. 11 Pore size distribution frequency of YS, CS and GS and samples after H_2SO_4/HNO_3 acid leaching test (named samples YS-S, CS-S, and GS-S in Fig. 9 and YS-N, CS-N, and GS-N in Fig. 10)

micropores and transition-pores increased in sample CS-S compared with those in CS. The measured porosity of sample GS-S was 9.58%, and the proportion of mesopores was nearly half of the pores.

Microscopic observations

The SEM images of secondary minerals (named samples YS-S salt, CS-S salt, and GS-S salt in Fig. 9 and GS-N salt in Fig. 10) are shown in Fig. 12. In the H_2SO_4 acid leaching test, clusters of spherical crystals of thenardite had precipitated on the mineral surfaces like cauliflower in YS-S (Fig. 12a–c). For CS-S, the secondary mineral was gypsum, which exhibited prismatic shape (Fig. 12d–f). For GS-S, the secondary minerals were gypsum. Under microscopic observations, the gypsum crystals exhibited tabular shape (Fig. 12g–i). In the HNO_3 acid leaching test, the gypsum crystals exhibited prismatic shape in GS-N (Fig. 12j–l).

Discussion

Influence of environment to the different decay of sandstone

In the salt resistance test, the decay processes of sandstones under three temperatures were different (Figs. 6–8). This can be attributed to the different hydration or crystallization stresses of mirabilite and thenardite. After drying at 105 °C for 16 h, sodium sulphate was in the phase of thenardite, which precipitated on the sandstone surface or in the pores. When cooling at 5 °C and 75% RH, superficial thenardite contacted with high water vapor and then was converted to mirabilite by means of hydration or crystallization [35]. Mirabilite tends to crystallize in large pores as euhedral micronsized crystals formed at low supersaturation near to the surface of the stone [36]. The precipitation of mirabilite on the surface generated sufficient stress to damage the superficial sandstone, which resulted in the disintegration of surface particle [37]. Therefore, the deterioration
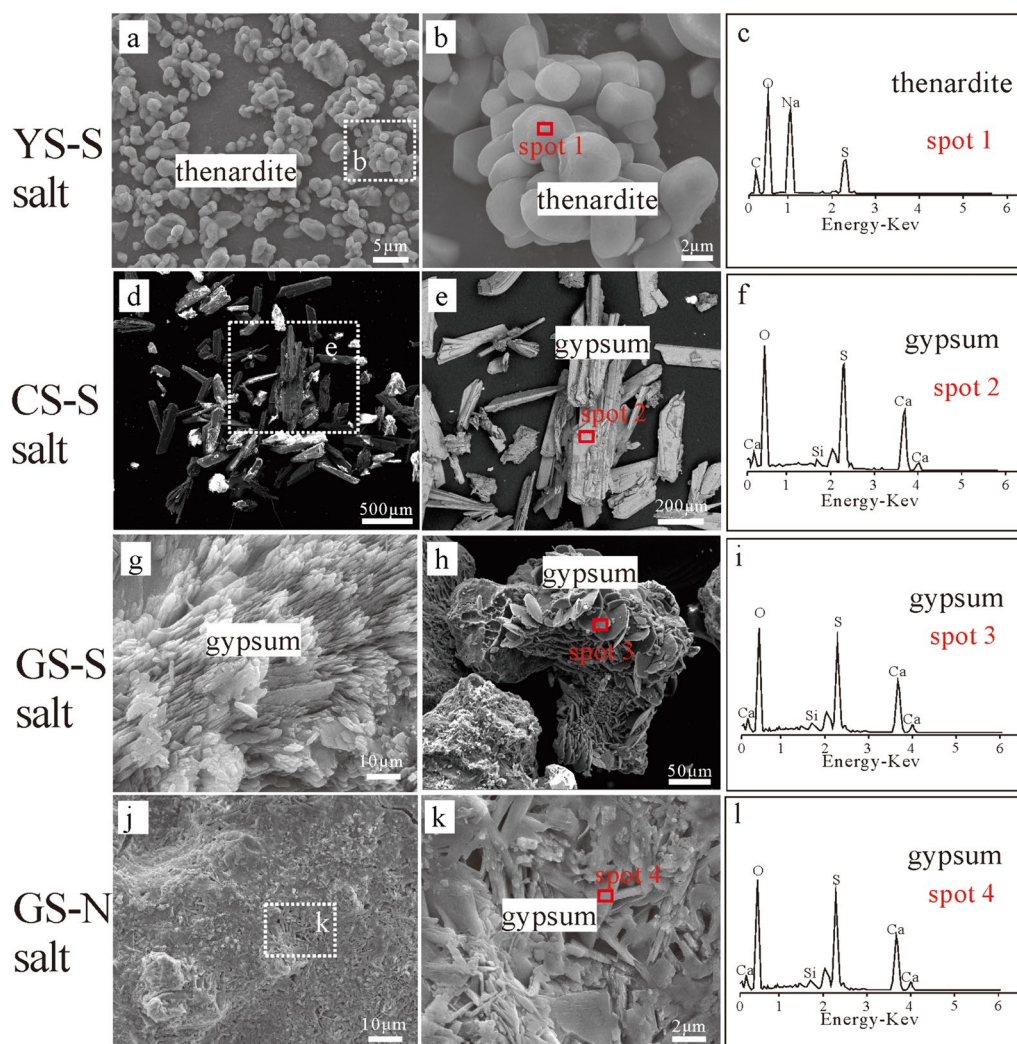
Zhang *et al. Heritage Science*   (2024) 12:244

Page 13 of 16

Fig. 12 SEM micrographs and EDS spectra of the salt crystals in acid leaching tests. **a**–**c** SEM images and EDS spectra of sample YS-S salt. **d**–**f** SEM images and EDS spectra of sample CS-S salt. **g**–**i** SEM images and EDS spectra of sample GS-S salt. **j**–**l** SEM images and EDS spectra of sample GS-N salt

patterns of YS, CS, and GS in the salt resistance test at 5 °C were rounding and crumbling (Fig. 6), which only destroyed the surface layer of sandstone. When cooling at 20 °C and 75% RH, there was a dynamic phase transformation between thenardite and mirabilite (Fig. 2). This process was much more damage than the single damage of thenardite or mirabilite [38, 39]. Therefore, the weight loss of sandstones in the salt resistance test at 20 °C was faster than those at 5 °C and 35 °C (Figs. 6–8). The deterioration patterns of YS, CS, and GS in the salt resistance test at 20 °C were contour scaling and crumbling (Fig. 7). This suggested that the crystallization of sodium sulfate took place deeper under the surface of the samples. When cooling at 35 °C & 75% RH, thenardite was the stable phase. The decay of sandstones was attributed to the

cyclic dissolution and precipitation of thenardite on the sandstone surface or in the pores. The deterioration patterns of YS, CS, and GS in the salt resistance test at 35 °C were crack and fragmentation (Fig. 8). These phenomena were induced by the crystallization pressure of thenardite, which generally crystallize within the pore or fissure spaces [26].

In the H_2SO_4/HNO_3 acid leaching test, YS, CS, and GS showed different deterioration patterns. In the H_2SO_4 acid leaching test, there were bulk efflorescences occurred on the surfaces of YS and CS (Fig. 9). However, there were not obvious variations for YS and CS in the HNO_3 acid leaching test (Fig. 10). Efflorescence and crust patterns developed in GS in the H_2SO_4 acid leaching test (Fig. 9). However, gypsum crust quickly formed in GS in

Zhang *et al. Heritage Science*   (2024) 12:244

Page 14 of 16

the HNO$_3$ acid leaching test (Fig. 10). Therefore, the solutional environment influenced the types and locations of the salt crystallization, which further controlled the consequent weathering patterns.

Influences of petrography and micro-structure to the different decay of sandstone

YS had the highest quartz concentration and lower clay minerals concentration (Table 1), which contributed to its well cementing strength than CS and GS. In addition, the highest porosity of YS leaded to its high ability of solution transport, as indicated by its performances in capillary absorption, water vapour diffusion, and evaporative drying tests (Figs. 4–5, 11). The better cementing strength and pore connectivity of YS leaded to that YS was the most resistant in the salt resistance test (Figs. 6–8). In addition, the good pore connectivity of YS can effectively transport salt solution to the surface during drying process. Therefore, thenardite efflorescence firstly crystallized on the side and then moved to the top of YS-S sample in the H$_2$SO$_4$ acid leaching test (Fig. 9).

CS had higher feldspar and calcite concentrations and lower quartz concentration than YS (Table 1). Therefore, the resistance of CS was worse than YS in the salt resistance test (Figs. 6–8). Even though YS and CS had similar porosity, the ability of solution transport for CS was worse than YS (Figs. 4–5, 11). This explained why efflorescence always crystallized on the side of cubic CS-S sample in the H$_2$SO$_4$ acid leaching test (Fig. 9). In addition, the higher calcite concentration of CS resulted in the formation of gypsum efflorescence on CS-S sample in the H$_2$SO$_4$ acid leaching test, rather than thenardite efflorescence as on YS-S (Fig. 12).

GS had the highest calcite and clay minerals concentrations (Table 1), which contributed to its worst cementing strength than YS and CS. The highest calcite concentration of GS contributed to the formation of gypsum crust in the HNO$_3$ acid leaching test, which were not observed in YS-N and CS-N (Fig. 10). The poor cementing strength and solution transport ability of GS leaded to its lowest salt resistance ability (Figs. 4, 5). In addition, the low pore connectivity of GS also resulted in that gypsum crystallized below the surface of cubic GS-S sample in the H$_2$SO$_4$ acid leaching test, which formed the subflorescences and the swelling of the top surface (Fig. 9). From YS to GS, the capillary water uptake height showed a decreasing trend. Therefore, in the H$_2$SO$_4$ acid leaching test, salts mainly crystalized on the top of cubic YS-S sample, on the side of cubic CS-S sample, and below the surface of cubic GS-S sample, respectively.

Subflorescence pattern developed in YS in the Nankan Grotto (Fig. 1c). At the field subflorescence pattern site, the salts were thenardite and secondary calcite [22]. This is different with the result of H$_2$SO$_4$ acid leaching test that the secondary mineral was thenardite in YS-S and formed efflorescence pattern (Fig. 9). Therefore, thenardite can crystallize on the surface as efflorescence and crystallize below the surface as subflorescence. In the Nankan Grotto, crust pattern developed in GS (Fig. 1e). The salts in the field crust pattern site were gypsum and secondary calcite [22]. The crusts developed in the siltstone of Taya Caves were also made of gypsum and minor calcite [40]. These are consistent with the performance of GS in the H$_2$SO$_4$ and HNO$_3$ acid leaching tests that gypsum formed crust (Figs. 9, 10). The secondary mineral was gypsum in CS-S and GS-S and gypsum formed efflorescence pattern (Fig. 9). In the statistical data about more than 300 samples of efflorescence on buildings and monuments in Saxony (Germany), gypsum is the most common salt in efflorescence [14]. In conclusion, gypsum can crystallize on the surface as efflorescence, or combine with primary minerals as crust. The differences in petrography and micro-structure of sandstones leaded to the differences in the types, amounts, and locations of the salt crystallization, which contributed to the different development of efflorescence, subflorescence, and crust patterns.

Implication for the protection of sandstone in the Nankan Grotto

Based on the above discussion, it is found that the deterioration patterns of YS, CS, and GS cannot be separated from the interaction with water. The water supply in the Nankan Grotto mainly comes from rainfall and is discharged in the forms of surface water and groundwater [23]. Therefore, rain shelter and drainage for the grottoes caved in YS, CS, and GS are both effective treatments. In addition, natural or synthetic hydrophobic compounds could be used to protect grottoes exposed to rain erosion [41, 42]. Based on the previous studies, an oligosuberamide bearing perfluoropolyether segments (FSB) and 3-perfluroether-amidopropylsilane (Si-PFE) are optimal protective agents for both low and highly porous stones due to their low surface tension [43, 44]. In addition, Si-PFE-TiO$_2$ is a more advanced material for the sustainable maintenance of building stones due to its durable superhydrophobicity and enhanced photocatalytic and antimicrobial properties [45]. Their water inhibition efficacy on YS, CS, and GS will be examined in the follow-up tests. In addition, the anisotropy of sandstone can have significant effects on the results of capillary water absorption and water vapour permeability. In these tests, there was a defect that the anisotropy of sandstone was not taken into account. In the further experiments, more attention will be paid on the anisotropy of sandstone for its water transport abilities.

Zhang *et al. Heritage Science*   (2024) 12:244

Page 15 of 16

The development of subflorescence in GS was more harmful to the grottoes. This pattern usually results in the detachment of the outer material. Therefore, the reinforcement between the outer loose material and the substrate is particularly critical. Inorganic or organic reinforcement materials could be used to fill large pores and cracks [46]. The cements in GS are mainly siliceous and calcareous materials. Therefore, nano-$Ca(OH)_2$ and nanosilica-based compounds maybe more suitable for the consolidation of the fragile stone surface in GS [47–50]. The consolidation efficacy of them will be verified in the following tests.

Conclusions

The mineralogical, major element, micro-structure analyses were conducted on three typical sandstones from the Nankan Grotto. In addition, salt resistance test and acid leaching test were conducted on them. The main conclusions are as follows.

1. The mineralogical compositions of YS, CS, and GS were quartz, feldspar, calcite, and clay minerals. The calcite and illite–smectite mixed layer concentrations in GS were much higher than those in YS and CS. YS and CS had similar properties of density, porosity, and unforced water absorption. However, GS had a higher density, lower porosity, and lower unforced water absorption than YS and CS. The water transport ability showed a decreasing trend from YS to GS.

2. In the salt resistance test, the decay processes of YS, CS, and GS under three temperatures were different. The decay of sandstones in the salt resistance test at 20 °C was faster than those at 5 °C and 35 °C. YS was the most resistant to the salt resistance test, followed by CS, and GS was the most vulnerable to the salt resistance test.

3. In the H_2SO_4 acid leaching test, YS, CS, and GS showed different deterioration patterns. For YS, the secondary mineral was thenardite and formed efflorescence pattern. For CS, the secondary mineral was gypsum and formed efflorescence pattern. For GS, the secondary mineral was gypsum, and efflorescence, subflorescence, and crust patterns occurred. In the HNO_3 acid leaching test, YS and CS did not show obvious variations. For GS, the secondary minerals were gypsum and dolomite, and crust pattern was observed. The porosity and proportion of macropores for YS, CS, and GS increased obviously after H_2SO_4 and HNO_3 acid leaching tests.

4. In general, efflorescence pattern was the most likely type of decay in YS and CS. Thenardite was the exclusive salt in the decay process of YS, while gypsum was the mainly salt in the decay process of CS. Gypsum crust and subflorescence were the most common types of decay for GS, and the salt weathering of GS was more severe than YS and CS. The results of this study improved our understanding of the constraints for different salt weathering processes. It also provides a reference for research on salt weathering and protection for other sandstone heritage sites.

Declarations

Ethics approval and consent to participate
Not applicable.

Consent for publication
Not applicable.

Competing interests
The authors declare no competing interests.

Author details
[1]Faculty of Geosciences and Engineering, Southwest Jiaotong University, Chengdu, Sichuan 611756, People's Republic of China. [2]Key Laboratory of Archaeological Exploration and Cultural Heritage Conservation Technology (Northwestern Polytechnical University), Ministry of Education, Xi'an, Shaanxi 710072, People's Republic of China. [3]Sichuan Province Engineering Technology Research Center of Ecological Mitigation of Geohazards in Tibet Plateau Transportation Corridors, Southwest Jiaotong University, Chengdu, Sichuan 611756, People's Republic of China.

References
1. Bonomo AE, Amodio AM, Prosser G, Sileo M, Rizzo G. Evaluation of soft limestone degradation in the Sassi UNESCO site (Matera, Southern Italy): loss of material measurement and classification. J Cult Herit. 2019;42:191–201.

Zhang *et al. Heritage Science*   (2024) 12:244

Page 16 of 16

2. Stück HL, Platz T, Müller A, Siegesmund S. Natural stones of the Saale-Unstrut region (Germany): petrography and weathering phenomena. Environ Earth Sci. 2018;77(8):300.
3. Dursun F, Topal T. Durability assessment of the basalts used in the Diyarbakır city walls, Turkey. Environ Earth Sci. 2019;78(15):456.
4. Zammit T, Cassar J. Investigating possible correlations between the porosimetry and insoluble residue content of Malta's Lower Globigerina Limestone. Bull Eng Geol Env. 2015;76(1):59–70.
5. Wang K, Xu G, Li S, Ge C. Geo-environmental characteristics of weathering deterioration of red sandstone relics: a case study in Tongtianyan Grottoes, Southern China. Bull Eng Geol Env. 2017;77(4):1515–27.
6. Török Á, Licha T, Simon K, Siegesmund S. Urban and rural limestone weathering; the contribution of dust to black crust formation. Environ Earth Sci. 2010;63(4):675–93.
7. Rihosek J, Bruthans J, Masin D, Filippi M, Carling GT, Schweigstillova J. Gravity-induced stress as a factor reducing decay of sandstone monuments in Petra, Jordan. J Cult Herit. 2016;19:415–25.
8. Liu X, Koestler R, Warscheid T, Katayama Y, Gu J. Microbial deterioration and sustainable conservation of stone monuments and buildings. Nat Sustain. 2020;3(12):991–1004.
9. Gázquez F, Calaforra J-M, Evans NP, et al. Physical weathering of carbonate host-rock by precipitation of soluble salts in caves: a case study in El Orón-Arco Cave (region of Murcia, SE Spain). Chem Geol. 2019;521:1–11.
10. Roussel E, Vautier F, Voldoire O, et al. Quantifying 450 years of limestone weathering induced by salt crystallization on fortifications in Malta and Gozo. Geomorphology. 2021;378:107614.
11. Sousa L, Siegesmund S, Wedekind W. Salt weathering in granitoids: an overview on the controlling factors. Environ Earth Sci. 2018;77(13):502.
12. Yan S, Xie N, Liu J, Li L, Peng L, Jiang S. Salt weathering of sandstone under dehydration and moisture absorption cycles: an experimental study on the sandstone from Dazu rock carvings. Earth Surf Proc Land. 2022;47(4):977–93.
13. Germinario L, Siegesmund S, Maritan L, Mazzoli C. Petrophysical and mechanical properties of Euganean trachyte and implications for dimension stone decay and durability performance. Environ Earth Sci. 2017;76(21):739.
14. Siedel H. Salt efflorescence as indicator for sources of damaging salts on historic buildings and monuments: a statistical approach. Environ Earth Sci. 2018;77(16):572.
15. Espinosa-Marzal RM, Scherer GW. Impact of in-pore salt crystallization on transport properties. Environ Earth Sci. 2013;69:2657–69.
16. Scherer GW. Crystallization in pores. Cem Concr Res. 1999;29(8):1347–58.
17. Steiger M. Crystal growth in porous materials—I: the crystallization pressure of large crystals. J Cryst Growth. 2005;282(3–4):455–69.
18. Yu S, Oguchi CT. Role of pore size distribution in salt uptake, damage, and predicting salt susceptibility of eight types of Japanese building stones. Eng Geol. 2010;115(3–4):226–36.
19. Martínez-Martínez J, Torrero E, Sanz D, Navarro V. Salt crystallization dynamics in indoor environments: stone weathering in the Muñoz chapel of the Cathedral of Santa María (Cuenca, central Spain). J Cult Herit. 2021;47:123–32.
20. Sun Q, Zhang Y. Combined effects of salt, cyclic wetting and drying cycles on the physical and mechanical properties of sandstone. Eng Geol. 2018;248:70–9.
21. Germinario L, Oguchi CT. Underground salt weathering of heritage stone: lithological and environmental constraints on the formation of sulfate efflorescences and crusts. J Cult Herit. 2021;49:85–93.
22. Zhang X, Ling S, Wu X, Xie J. Microscopic weathering mechanisms of subflorescence and crust patterns in the Nankan Grotto, northern Sichuan, China. Herit Sci. 2023;11:181.
23. Zhang X, Ling S, Wu X, et al. Hydrochemistry process and microweathering behaviour of sandstone heritages in the Nankan Grotto, China: insights from field micro-observations and water–rock interaction experiments. Bull Eng Geol Env. 2023;82:356.
24. Zhang X, Wu X, Ling S, et al. Microscopic weathering characteristics and deterioration mechanisms of sandstone in the Nankan Grotto, northern Sichuan, China. Bull Eng Geol Env. 2024;83:219.
25. Angeli M, Bigas J-P, Benavente D, Menéndez B, Hébert R, David C. Salt crystallization in pores: quantification and estimation of damage. Environ Geol. 2006;52(2):205–13.
26. Rodriguez-Navarro C, Doehne E, Sebastian E. How does sodium sulfate crystallize? Implications for the decay and testing of building materials. Cem Concr Res. 2000;30(10):1527–34.
27. Steiger M, Asmussen S. Crystallization of sodium sulfate phases in porous materials: the phase diagram Na_2SO_4–H_2O and the generation of stress. Geochim Cosmochim Acta. 2008;72(17):4291–306.
28. Ling S, Wu X, Zhao S, Liao X. Evolution of porosity and clay mineralogy associated with chemical weathering of black shale: a case study of Lower Cambrian black shale in Chongqing, China. J Geochem Explor. 2018;188:326–39.
29. Ling S, Wu X, Sun C, Liao X, Ren Y, Li X. Mineralogy and geochemistry of three weathered Lower Cambrian black shale profiles in Northeast Chongqing, China. Geosci J. 2016;20(6):793–812.
30. GB/T50266. Standard for test methods of engineering rock mass. 2013.
31. GB/T9966.13. Test methods for natural stone—Part 13: Determination of water absorption coefficient by capillarity. 2021.
32. Ruedrich J, Bartelsen T, Dohrmann R, Siegesmund S. Moisture expansion as a deterioration factor for sandstone used in buildings. Environ Earth Sci. 2011;63(7–8):1545–64.
33. GB/T17146. Test methods for water vapour transmission properties of building materials and products. 2015.
34. Zhang Y, Zhang Y, Huang J. Experimental study on capillary water absorption of sandstones from different grotto heritage sites in China. Herit Sci. 2022;10(1):25.
35. Thaulow N, Sahu S. Mechanism of concrete deterioration due to salt crystallization. Mater Charact. 2004;53(2–4):123–7.
36. Ruiz-Agudo E, Mees F, Jacobs P, Rodriguez-Navarro C. The role of saline solution properties on porous limestone salt weathering by magnesium and sodium sulfates. Environ Geol. 2007;52(2):269–81.
37. Flatt RJ. Salt damage in porous materials: how high supersaturation is generated. J Cryst Growth. 2002;242:435–54.
38. Rodriguez-Navarro C, Doehne E. Salt weathering: influence of evaporation rate, supersaturation and crystallization pattern. Earth Surf Proc Land. 1999;24:191–209.
39. Tsui N, Flatt RJ, Scherer GW. Crystallization damage by sodium sulfate. J Cult Herit. 2003;4(2):109–15.
40. Germinario L, Oguchi CT, Tamura Y, Ahn S, Ogawa M. Taya Caves, a Buddhist marvel hidden in underground Japan: stone properties, deterioration, and environmental setting. Herit Sci. 2020;8(1):87.
41. Cao Y, Salvini A, Camaiti M. Oligoamide grafted with perfluoropolyether blocks: a potential protective coating for stone materials. Prog Org Coat. 2017;111:164–74.
42. Cao Y, Salvini A, Camaiti M. Facile design of "sticky" near superamphiphobic surfaces on highly porous substrate. Mater Des. 2018;153:139–52.
43. Cao Y, Salvini A, Camaiti M. One-step fabrication of robust and durable superamphiphobic, self-cleaning surface for outdoor and in situ application on building substrates. J Colloid Interface Sci. 2021;591:239–52.
44. Cao Y, Salvini A, Camaiti M. Superhydrophobic fluorinated oligomers as protective agents for outdoor stone artworks. J Cult Herit. 2020;44:90–7.
45. Cao Y, Salvini A, Camaiti M. Multi-functional TiO_2-based nanocomposite coating with durable superhydrophobicity and enhanced photocatalytic and antimicrobial properties for the sustainable maintenance of building stones. Constr Build Mater. 2023;404: 133139.
46. Zhu J, Zhang P, Ding J, et al. Nano $Ca(OH)_2$: a review on synthesis, properties and applications. J Cult Herit. 2021;50:25–42.
47. Borsoi G, Lubelli B, Rv H, Veiga R, Silva AS. Understanding the transport of nanolime consolidants within Maastricht limestone. J Cult Herit. 2016;18:242–9.
48. Borsoi G, Lubelli B, Hees RV, Veiga R, Silva AS. Evaluation of the effectiveness and compatibility of nanolime consolidants with improved properties. Constr Build Mater. 2017;142:385–94.
49. Cao Y, Camaiti M, Endrizzi M, Forti G, Vergani E, Forti I. Enhanced consolidation efficacy and durability of highly porous calcareous building stones enabled by nanosilica-based treatments. Sci China Technol Sci. 2023;66:2197–212.
50. Zhu J, Li X, Zhang Y, et al. Dual functionalities of few-layered boron nitrides in the design and implementation of $Ca(OH)_2$ nanomaterials toward an efficient wall painting fireproofing and consolidation. ACS Appl Mater Interfaces. 2019;11:11792–9.

Publisher's Note